Investigation of the influence of orientation on critical heat flux for flow boiling with two-phase inlet

Christopher Konishi [a], Issam Mudawar [a,*], Mohammad M. Hasan [b]

[a] Boiling and Two-Phase Flow Laboratory (BTPFL), School of Mechanical Engineering, Purdue University, 585 Purdue Mall, West Lafayette, IN 47907, USA
[b] NASA Glenn Research Center, 21000 Brookpark Road, Cleveland, OH 44135, USA

ARTICLE INFO

ABSTRACT

This study explores the mechanism of flow boiling critical heat flux (CHF) for FC-72 in a rectangular channel fitted along one side with a heated wall. The flow is supplied as a two-phase mixture and the channel is tested at different orientations relative to Earth's gravity. High-speed video imaging is used to identify the CHF trigger mechanism for different orientations, mass velocities and inlet qualities. It is shown that orientation has a significant influence on CHF for low mass velocities and small inlet qualities, with the orientations surrounding horizontal flow with downward-facing heated wall causing stratification of the vapor towards the heated wall and yielding very small CHF values. High mass velocities cause appreciable diminution in the influence of orientation on CHF, which is evidenced by similar flow patterns and CHF trigger mechanism regardless of orientation. The interfacial lift-off model is shown to predict the influence of orientation on CHF with good accuracy. Overall, this study points to the effectiveness of high mass velocities at combating buoyancy effects and helping produce CHF values insensitive to orientation.

1. Introduction

1.1. Importance of two-phase flow and heat transfer to future space missions

As the attention of space agencies worldwide is shifting to more complex and more distant missions, including manned missions to Mars, greater emphasis is being placed on efficiency of power utilization onboard both space vehicles and future planetary bases. A key tactic towards achieving this goal is to reduce the weight and volume of all subsystems. These include several components that are intended specifically for thermal management. One means to achieving this goal is to transition from single-phase to two-phase thermal management. By capitalizing upon the merits of latent heat of the working fluid rather than sensible heat alone, two-phase systems are expected to yield orders of magnitude enhancement in evaporation and condensation heat transfer coefficients compared to single-phase systems, which would result in drastic reductions in the weight and volume of thermal management hardware [1].

Thermal management plays a crucial role in supporting astronaut life onboard space vehicles and planetary bases. Thermal management systems are responsible for controlling the temperature and humidity of the environment using a Thermal Control System (TCS), and fall into three main categories [2]. *Heat acquisition* components acquire energy from a heat-producing source. *Heat transport* components move the energy from the heat acquisition component to heat rejection hardware. *Heat rejection* components reject the heat from the TCS to deep space by radiation. There are also other specialized subsystems, such as *refrigerator/freezer* components that provide cooling for science experiments and food storage, and *water recovery* components that transfer crew and system wastewater into potable water for crew and system reuse.

Understanding the influence of gravity on two-phase flow and heat transfer is crucial to the development of space power for future missions. For example, NASA's Fission Power System (FPS) program aims to develop a fission system for use on advanced science missions, which would provide both very high power and very low mass to power ratio [3]. The Rankine cycle is one example of a high power system (>100 kW) that promises high thermal efficiency and enables high performance nuclear electric propulsion for distant cargo and human missions. But before the Rankine cycle can achieve fruition, the influence of microgravity on fluid physics must be well understood. This includes critical heat flux (CHF) in the boiler, and shear driven condensation heat transfer.

1.2. Influence of gravity

The influence of gravity is exasperated in a two-phase system by the large density difference between liquid and vapor. This difference plays a crucial role in dictating the motion of vapor relative

* Corresponding author. Tel.: +1 (765) 494 5705; fax: +1 (765) 494 0539.
  E-mail address: mudawar@ecn.purdue.edu (I. Mudawar).
  URL: https://www.engineering.purdue.edu/BTPFL (I. Mudawar).

Nomenclature

A	cross-sectional area of flow channel
A_w	area of wetting front
b	ratio of wetting front length to wavelength
c	wave speed
$C_{f,i}$	interfacial friction coefficient
c_p	specific heat at constant pressure
D	diameter
f	friction factor
G	mass velocity
g_e	Earth gravity
H	height of flow channel; layer thickness
h_{fg}	latent heat of vaporization
k	wave number
$\dot{m}$	mass flow rate
$\dot{m}'_{fg}$	liquid evaporation rate between heated wall liquid and vapor layers
p	pressure
P_e	electric power input to second preheater
P_i	interfacial perimeter
P_w	perimeter in contact with channel walls
q''	wall heat flux
q''_m	critical heat flux
Re	Reynolds number
T	temperature
t	time
U	mean axial velocity
u_i	interfacial velocity
W	width of flow channel
x_e	thermodynamic equilibrium quality
x_f	liquid mass flow fraction
y	coordinate normal to heated wall
z	axial distance
z_0	axial location where vapor layer velocity just exceeds liquid layer velocity

$z*$	axial location for determining vapor layer thickness and critical wavelength in Interfacial lift-off model

Greek symbols

α	vapor (area-based) void fraction
δ	vapor layer thickness
e_f	liquid area fraction
h	interfacial perturbation
q	flow orientation angle
λ_c	critical wavelength
μ	dynamic viscosity
ρ	density
ρ''	modified density
σ	surface tension
τ_i	interfacial shear stress
τ_w	wall shear stress

Subscripts

1	insulated wall liquid layer
2	middle vapor core
3	heated wall liquid layer
4	heated wall wavy vapor layer
exp	experimental (measured)
f	saturated liquid
g	saturated vapor
i	interface
in	inlet to heated portion of flow channel
k	phase k, $k = g$ or f
n	normal to heated wall
$pred$	predicted
$preh$	upstream of second preheater
w	wall; wetting front.

to liquid, thereby influencing heat transfer effectiveness. Flow boiling CHF is an important heat transfer design parameter that exhibits complex variations with the magnitude of gravitational field. The challenge in designing a thermal management system is to make certain that the prevailing boiling heat flux is safely below CHF, which explains the importance space system design engineers place on precise determination of the influence of both flow conditions and gravity on CHF. This is especially the case for high-flux, heat-flux-controlled electronic and power devices, where CHF occurrence can lead to device burnout or other forms of permanent damage. This risk explains a recent surge in the number of published articles addressing means to enhance CHF using a variety of configurations, including spray [4–7], jet [8–11], and micro-channel cooling schemes [4,12–15], and surface enhancement techniques [16].

A key strategy in designing two-phase components for space missions is to develop tools that enable the prediction of flow conditions (e.g., coolant flow rate) that would ensure insensitivity of evaporation or condensation to gravity [1,17,18] for the relevant gravity range important to a particular space system or mission, as illustrated in Fig. 1. This would allow existing data, correlations, and models developed from ground-based $1 - g_e$ studies to be employed with confidence for design of reduced gravity and microgravity thermal management systems.

Researchers employ a variety of techniques to assess the important influence of gravity on flow boiling CHF. These include conducting ground-based experiments at different flow orientations relative to Earth's gravity [17,18]. Microgravity is achieved in drop tower and drop shaft experiments, which provide a high degree of control of residual gravity, but are too short (less than 10 s) to achieve steady two-phase flow or to collect sufficient amounts of data for statistical analysis without a significant number of repetitive drops [2]. Aircraft parabolic flight tests offer significant advantages over drop tower and drop shaft tests, including longer test duration (up to 25 s), larger and more complex test packages, and ability of the experimenter to interact with the test [1]. Space Shuttle experiments provided an ideal testing environment because of the ability to accommodate long-duration experiments with good control of residual gravity. Since the recent abandonment of Space Shuttles, the International Space Station (ISS) has become the sole platform for conduction long duration microgravity experiments.

Researchers at the Purdue University Boiling and Two-Phase Flow Laboratory (PU-BTPFL) have been involved in several NASA-supported initiatives to explore the influence of gravity on both flow boiling and condensation. These studies are initiated with ground experiments, by exploring the effects of flow orientation relative to Earth's gravity [17,18]. The same hardware is then tested in parabolic flight experiments [1]. Both types of tests are used to assist the design of test hardware for future experiments onboard the ISS. The present study concerns flow boiling CHF findings from ground-based $1 - g_e$ experiments.

1.3. Mechanisms of flow boiling CHF

Four different mechanisms have been proposed to trigger flow boiling CHF: *Boundary Layer Separation*, *Bubble Crowding*, *Sublayer*
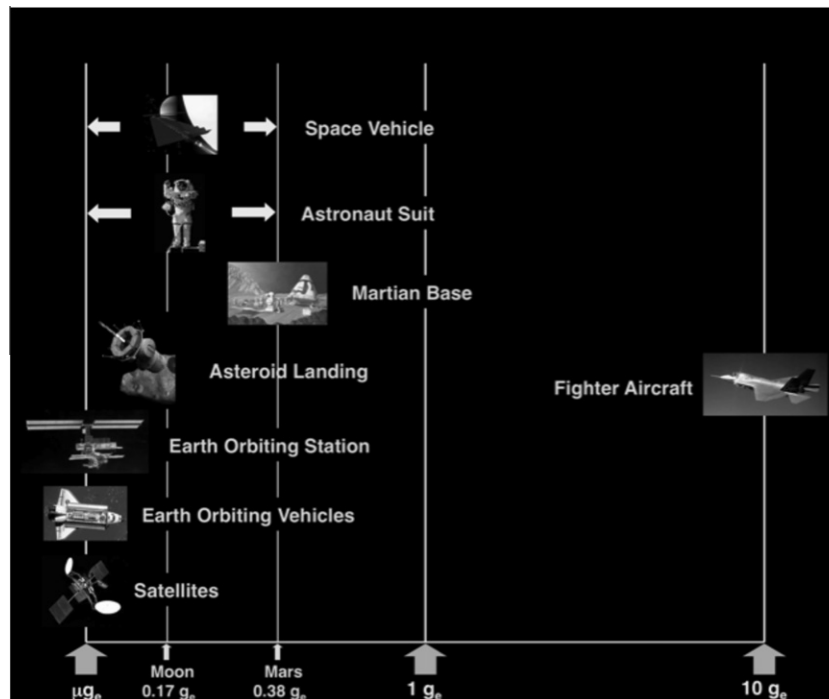
Fig. 1. Examples of systems demanding predictive models of the effects of gravity on two-phase flow and heat transfer.

Dryout, and *Interfacial Lift-off*. The Boundary Layer Separation Model is built on the hypothesis that CHF will occur when the rate of vapor production normal to a heated wall attains a critical value that triggers a sharp reduction in liquid velocity gradient near the wall, which precipitates separation of the liquid from the wall [19,20]. The Bubble Crowding Model is based on the premise that CHF occurs when the bubbly wall layer becomes too thick to permit turbulent fluctuations in the core liquid to supply a sufficient amount of liquid to the wall [21,22]. The Sublayer Dryout Model is based on the premise that, near CHF, the wall is cooled by a thin sublayer that forms beneath oblong, coalescent vapor bubbles at the wall, and that CHF will occur when heat from the wall exceeds the enthalpy of bulk liquid replenishment of the sublayer [23]. The interfacial lift-off model [24,25] is built upon the observation that, prior to CHF, the vapor coalesces into a fairly continuous but wavy vapor layer at the wall. The wavy interface makes contact with the heated wall in 'wetting fronts' corresponding to the wave troughs, which provide partial cooling of the wall. The trigger mechanism for CHF according to the interfacial lift-off model is 'lift-off' of the wetting fronts from the wall due to intense vapor effusion.

It is important to note that the majority of flow boiling CHF studies have been conducted in vertical upflow, where buoyancy plays the important role of assisting the removal of coalescent vapor masses from the wall. The vapor removal, liquid replenishment of the wall, and CHF mechanism are greatly altered when the flow channel is rotated away from the vertical upflow orientation. Zhang et al. [17,18] examined the influence of flow orientation for flow boiling with zero inlet vapor void in a rectangular channel that was heated along one side. They observed several distinct mechanisms for CHF depending on the combined effects of flow velocity, flow orientation, and placement of the heated wall relative to gravity. The influence of orientation was especially significant at low inlet liquid velocities, where buoyancy could overcome the drag forces exerted by the liquid on the coalescent vapor bubbles; the drag forces are essential to both the vapor removal and liquid replenishment of the wall. This observation is in general agreement with several prior studies involving the influence of flow orientation on CHF [26–28]. At low velocities, CHF for

horizontal flow with an upward-facing heated wall resembled pool boiling. On the other hand, CHF for horizontal flow with a downward-facing heated wall resulted in stratification of vapor above liquid. CHF for the downflow orientation was highly dependent on the relative magnitude of buoyancy and liquid drag, and was triggered by flooding when the buoyancy overcame the drag force. The detrimental influence of buoyancy was evidenced by CHF values for certain orientations being much smaller than those for vertical upflow. For vertical upflow, CHF was dominated by only one mechanism, interfacial lift-off. The complex influence of orientation on CHF encountered at low velocities was virtually eliminated above a threshold velocity. Above this threshold, the Interfacial Lift-off mechanism was observed for all orientations and virtually identical CHF values were measured regardless of orientation. In a subsequent study, Zhang et al. performed similar flow boiling experiments in parabolic flight to simulate microgravity [1]. In the absence of buoyancy, CHF was triggered by interfacial lift-off even at the low velocities that precipitated the afore-mentioned complex regimes in the ground experiments.

Recently, Kharangate et al. extended the ground tests of Zhang et al. [17,18] to operating conditions where the fluid entered the channel in saturated state with finite vapor void for vertical upflow [29] and horizontal flow with the heated wall upward-facing [30]. The inlet void caused an appreciable increase in liquid velocity along the flow channel, which increased the magnitude of liquid drag forces. Despite the complicated flow pattern caused by the incoming two-phase mixture, CHF for both orientations was predicted with good accuracy using a modified form of the interfacial lift-off model.

The present study is a continuation of the ground-based studies of flow boiling CHF for different orientations begun by Zhang et al. [17,18] for subcooled and saturated liquid inlet conditions, and the more recent vertical and horizontal studies by Kharangate et al. [29,30] for saturated two-phase mixture inlet conditions. The present study is focused on saturated two-phase mixture inlet conditions similar to those in [29,30], but covers all flow orientations relative to Earth's gravity. Saturated inlet conditions are important for space applications where a number of heat dissipating

electronic or power modules are cooled in series using a single two-phase flow loop. While upstream modules can take advantage of subcooled flow boiling, both the sensible and latent heat of the coolant are gradually depleted, and the downstream modules may be exposed to a two-phase mixture. In the present study, high-speed video imaging is used to capture interfacial behavior at wall heat fluxes up to and including CHF. The primary objectives of the present study are to: (1) identify CHF mechanisms associated with different orientations for varying mass velocity and inlet quality, and (2) explore the effectiveness of the interfacial lift-off model in predicting the new CHF data.

2. Experimental methods

2.1. Flow loop

Fig. 2(a) shows a schematic of the two-phase flow loop that is configured to condition the working fluid, FC-72, to the desired pressure, mass velocity, and quality at the inlet to the main flow boiling test module. The bulk of the FC-72 liquid is contained in a reservoir that is fitted with both an electrical immersion heater and a water-cooled condensation coil. Prior to testing, the FC-72 is de-aerated by vigorous boiling with the aid of the immersion heater. The non-condensable gases are purged to the ambient using a vacuum pump as the FC-72 is recaptured by condensation in the upper part of the reservoir. The coolant is circulated through the flow loop using a gear pump. Exiting the pump, the coolant passes through a filter followed by a turbine flow meter. The liquid then enters two in-line electric heaters – preheaters – connected in series before entering the flow boiling module. Each of the in-line heaters is powered by a 115-W variac to regulate power input to the liquid. The first preheater raises the liquid temperature to a level close to, but below saturation temperature, while the second preheater heats the fluid to a saturated mixture with a prescribed quality at the inlet to the flow boiling module. The quality at the inlet to the flow boiling module is determined from measurements of liquid temperature, T_{preh}, and pressure, p_{preh}, upstream of the second preheater, and electrical power input, P_e, to the second pre-heater according to the relation

$$x_{e,in} = -\frac{c_{p,f}(T_{sat} - T_{preh})}{h_{fg}} + \frac{P_e}{\dot{m}h_{fg}}. \tag{1}$$

In Eq. (1), T_{sat} is the coolant saturation temperature corresponding to the pressure measured upstream of the preheater.

Exiting the flow boiling module, the two-phase mixture is passed through an air-cooled heat exchanger to return the fluid to liquid state. A nitrogen-filled accumulator is situated between the heat exchanger and the reservoir to provide a controlled reference pressure point for the entire loop. The accumulator contains stainless steel bellows that accommodate any expansion or contraction of the FC-72.

2.2. Flow boiling module

The flow boiling test module is designed to conduct flow boiling CHF measurements and allow video motion analysis of the two-phase flow along a uniformly heated wall. As shown in Fig. 2(b), the flow boiling module consists of two transparent polycarbonate plastic (Lexan) plates that are bolted together between two stainless steel support plates; the purpose of the latter plates is help prevent buckling of the plastic plates or fluid leaks. A rectangular flow channel is formed by milling a 5.0-mm high by 2.5-mm wide slot into the top plastic plate. A portion of the opposite plastic plate is milled out to insert a 0.56-mm thick, 6.5-mm wide and 101.6-mm long oxygen-free copper plate that serves as the heated wall

for the flow boiling module. The heated plate is positioned 106 hydraulic diameters from the inlet to help ensure fully developed flow at the upstream edge of the heated wall. A honeycomb insert is affixed upstream of the channel inlet to break up any large inlet eddies and help straighten the flow. A flexible Teflon cord is trapped in an o-ring groove between the two plastic plates to prevent any leaks. The interface between the copper plate and the lower plastic plate is sealed with high-temperature silicone rubber.

As shown in Fig. 2(c), the copper wall is heated by a series of six 4.0-mm wide and 16.1-mm long thick-film resistors. The resistors are soldered to the underside of the copper plate and connected in a parallel electrical circuit, powered by a single 115-V variac. The resistors are carefully selected from a batch of resistors to match an exact electrical resistance of 188 Ω to ensure uniform heat flux along the copper wall. The copper wall temperature is measured by a series of five type-K thermocouples that are inserted in small shallow holes between the resistors. As discussed in [1], this heated wall design ensures both reliable CHF measurement and fast temperature response, typically in less than 5 s. Fluid temperature and pressure are measured by type-K thermocouples and pressure transducers, respectively, both upstream and downstream of the heated wall.

The test module is mounted on an aluminum bracket that features a 0-360° swivel. This bracket, along with the flow loop components, power and instrumentation cabinets, and data acquisition system, are mounted in a single rigid aluminum frame.

2.3. Flow visualization techniques

A Photron Fastcam Ultima APX camera system, which has a shutter speed of 1/20,000 s, is used to capture interfacial behavior along the flow boiling channel at a frame rate of 4000 fps. High magnification is achieved with the aid of a Nikon Micro-Nikkor 105 mm f/8D autofocus lens. The camera is positioned normal to the side of the flow-channel, backlit from behind the channel. Video imaging is performed at the inlet, middle, and outlet portions of the heated wall at various heat fluxes up to and including CHF. Each of the video images presented in this study corresponds to approximately one-fifth the length of the heated wall.

2.4. Operating conditions and measurement accuracy

Flow boiling tests are performed in eight flow orientations as illustrated in Fig. 3. For all the orientations, the flow radiates outwards, and the placement of the heated wall (indicated by a black rectangular strip), along with the flow orientation, produce predominantly upflow or downflow with the heated wall facing either upwards or downwards relative to Earth's gravity. For each orientation, tests are attempted at nine values of mass velocity, with G/ρ_f = 0.126, 0.224, 0.315, 0.398, 0.542, 0.712, 0.850, 0.995 and 1.130 m/s. Pressure at the outlet from the heated wall is held constant at 103 kPa (15 psia) for all the tests. For each mass velocity, the inlet temperature and outlet pressure are first adjusted to desired values, and the preheater power, P_e, is progressively increased to span an inlet quality range of $x_{e,in}$ = 0.01 − 0.19.

During the tests, the electrical power input to the heated wall is increased in small increments and the electrical power, flow rate, temperature and pressure measurements are recorded only after conditions in the flow boiling channel and entire flow loop reach steady state. This procedure is repeated up to CHF, which takes the form of a sudden unsteady rise in wall temperature initiated at any of the wall thermocouple locations.

Pressure is measured both upstream and downstream of the heated wall of the flow boiling module as well as at other locations along the loop by pressure transducers having an accuracy of 0.01%. Temperatures are measured along the heated wall as well
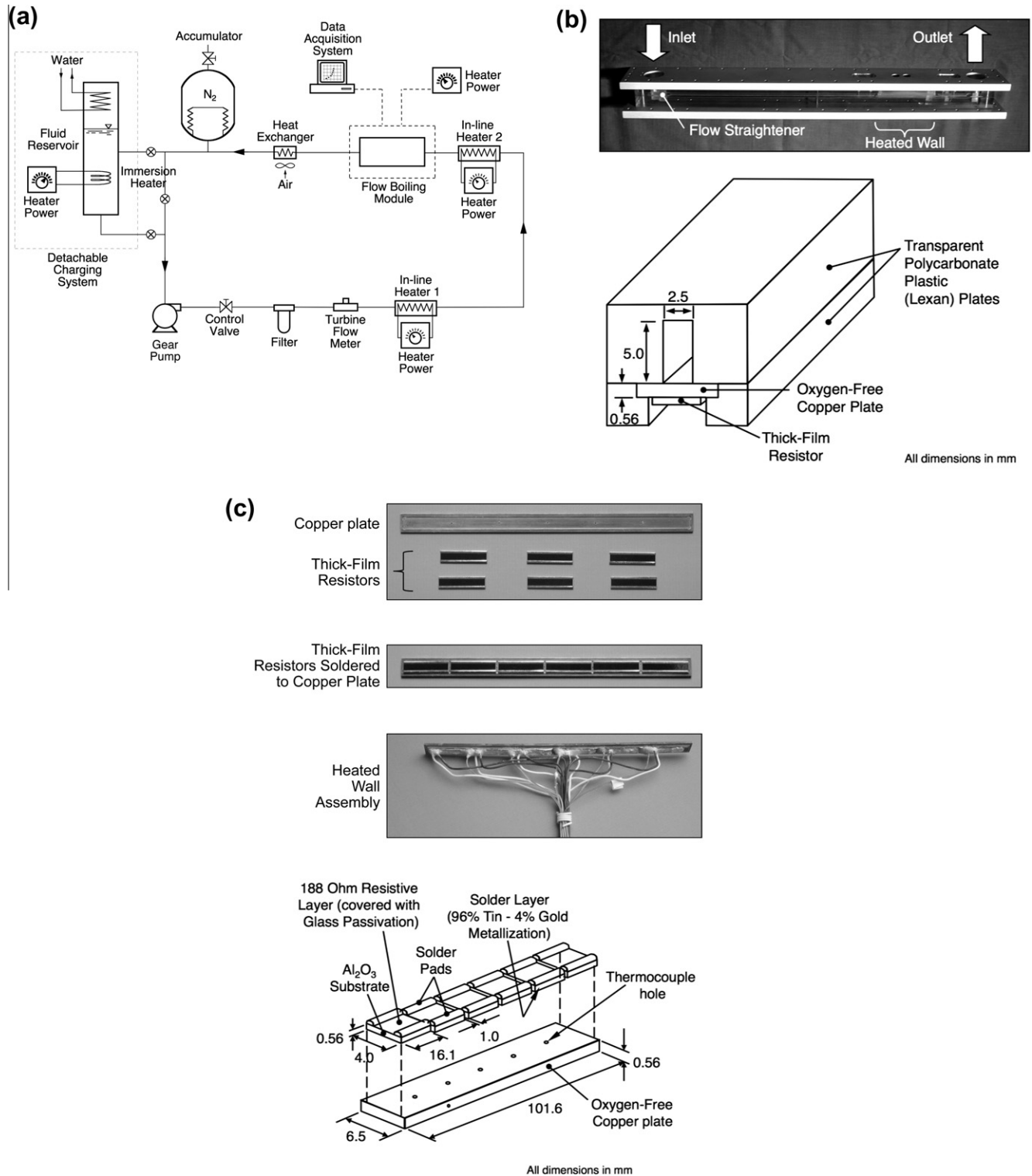
(a)

(b)

(c)

All dimensions in mm

Fig. 2. (a) Schematic of two-phase flow loop. (b) Flow channel assembly. (c) Construction of heated wall.

as upstream and downstream of the heated wall and at various points along the loop using type-K thermocouples with an uncertainty of 0.3 °C. The uncertainty in the heat flux measurement is 0.2%.

3. Flow visualization results

Emphasis during the flow visualization experiments is placed on capturing interfacial behavior at conditions that precede CHF

in order to identify the CHF trigger mechanism. These conditions are captured at about 95% CHF (termed CHF– hereafter) to avoid the risk of physical wall burnout.

Fig. 4(a) shows a polar composite of photos captured in the outlet region of the heated portion of the channel at CHF– for $G/\rho_f = 0.224$ m/s and inlet quality of $x_{e,in} = 0.01$. There are similarities in CHF mechanism corresponding to certain ranges of orientation angles. The first range includes $\theta = 315°$, $0°$, and $45°$, orientations surrounding horizontal flow with upward-facing heated wall.
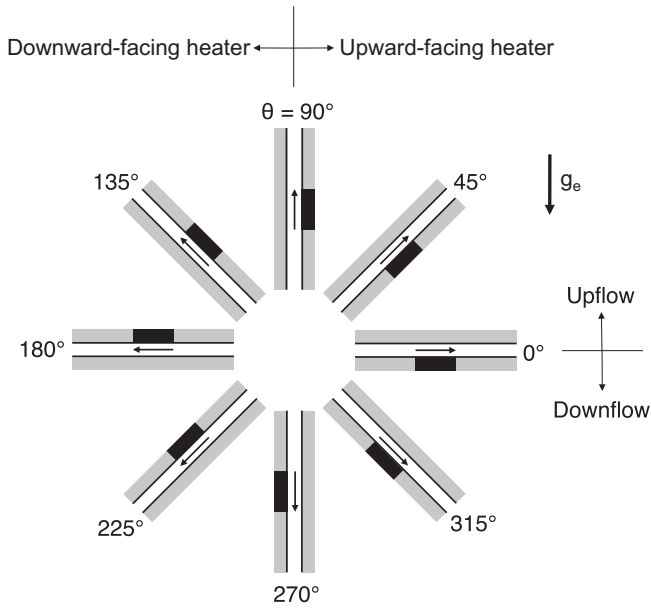
Fig. 3. Flow orientation nomenclature. Heater location for each orientation is indicated by a black rectangular strip.

Buoyancy causes clear separation between the phases at the channel inlet, with the vapor residing above the liquid, and this separation persists along the heated portion of the channel. At CHF-, there is appreciable vapor production within the liquid layer flowing along the heated wall. CHF appears to be triggered by the vapor beginning to separate the liquid layer from the wall. For $\theta = 90°$, corresponding to vertical upflow, the flow enters the flow separated, with liquid covering both the heated wall and opposite insulated wall, as well as the front and back walls, surrounding a central vapor core. This pattern persists along the heated portion of the channel, but with the liquid layer along the heated wall undergoing appreciable vapor production. Here too, CHF occurs

when the vapor production causes separation of the liquid layer adjacent to the heated wall. For $\theta = 135°$, $180°$ and $225°$, orientations surrounding horizontal flow with downward-facing heated wall, there is clear stratification of vapor above liquid, which starts at the channel inlet and persists along the heated portion of the channel. With the vapor layer covering the heated wall, CHF for these orientations is quite small, especially for $\theta = 225°$, which culminates in a vanishingly small CHF value of only 1.85 W/cm^2. For $\theta = 270°$, corresponding to vertical downflow, like vertical upflow, the flow enters the flow with liquid covering the heated wall, opposite insulated wall, and front and back walls, surrounding a central vapor core. This pattern also persists along the heated portion of the channel, and CHF occurs when vapor production begins to separate the liquid layer adjacent to the heated wall. Despite seemingly identical flow patterns, there is a fundamental difference between the flows for $\theta = 90°$ and $\theta = 270°$ because of the buoyancy serving to assist vapor removal along the channel for the former and resist the vapor removal for the latter. This difference is responsible for the $\theta = 270°$ orientation producing lower CHF, 10.3 W/cm^2, compared to that for $\theta = 90°$, 13.7 W/cm^2.

Interfacial flow behavior for $\theta = 270°$ is especially complex for flow boiling systems. In a previous study by Zhang et al. [17] involving CHF with the coolant entering the channel in pure liquid state, three possible CHF regimes were observed at $\theta = 270°$ at low flow velocities. At 0.1 m/s, strong buoyancy effects overcame any drag or shear forces exerted by the liquid, causing the vapor to flow backwards (i.e., vertically upwards) along the channel. As the flow velocity was increased, a balance was achieved between the buoyancy and liquid forces, causing the vapor to stagnate along the channel. Increasing the liquid velocity further caused the liquid drag and shear forces to exceed buoyancy, and the vapor to flow concurrently with the liquid. Interestingly, only the third concurrent vapor flow regime is observed in the present study, apparently because of the increasing magnitude of effective liquid velocity and therefore the liquid drag and shear forces when the fluid is supplied to the channel as a two-phase mixture rather than pure liquid.

Fig. 4(b) shows a polar composite of photos captured in the outlet region of the heated portion of the channel at CHF- for a higher
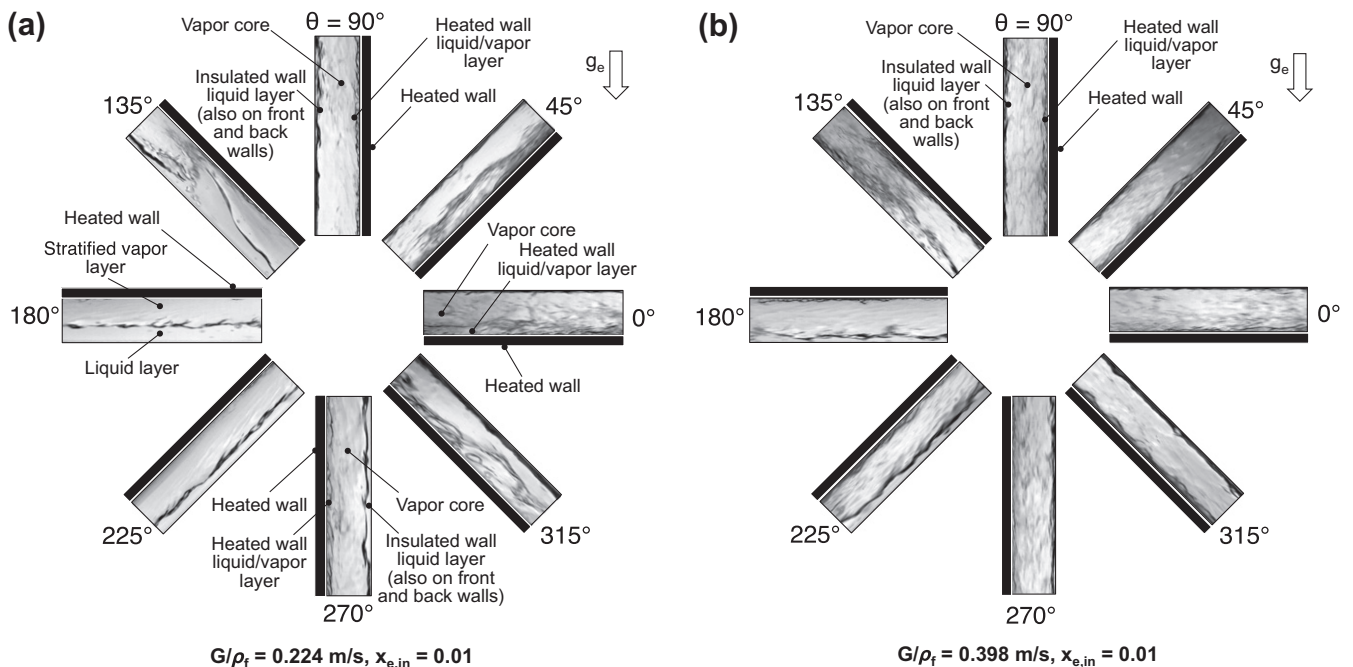

Fig. 4. Photos of interfacial behavior captured in the outlet region of the heated portion of the channel at CHF- for different flow orientation for (a) $G/\rho_f = 0.224$ m/s and $x_{e,in} = 0.01$, and (b) $G/\rho_f = 0.398$ m/s and $x_{e,in} = 0.01$.

(a)

G/ρ_f = 0.224 m/s, $x_{e,in}$ = 0.01

(b)

G/ρ_f = 0.398 m/s, $x_{e,in}$ = 0.01

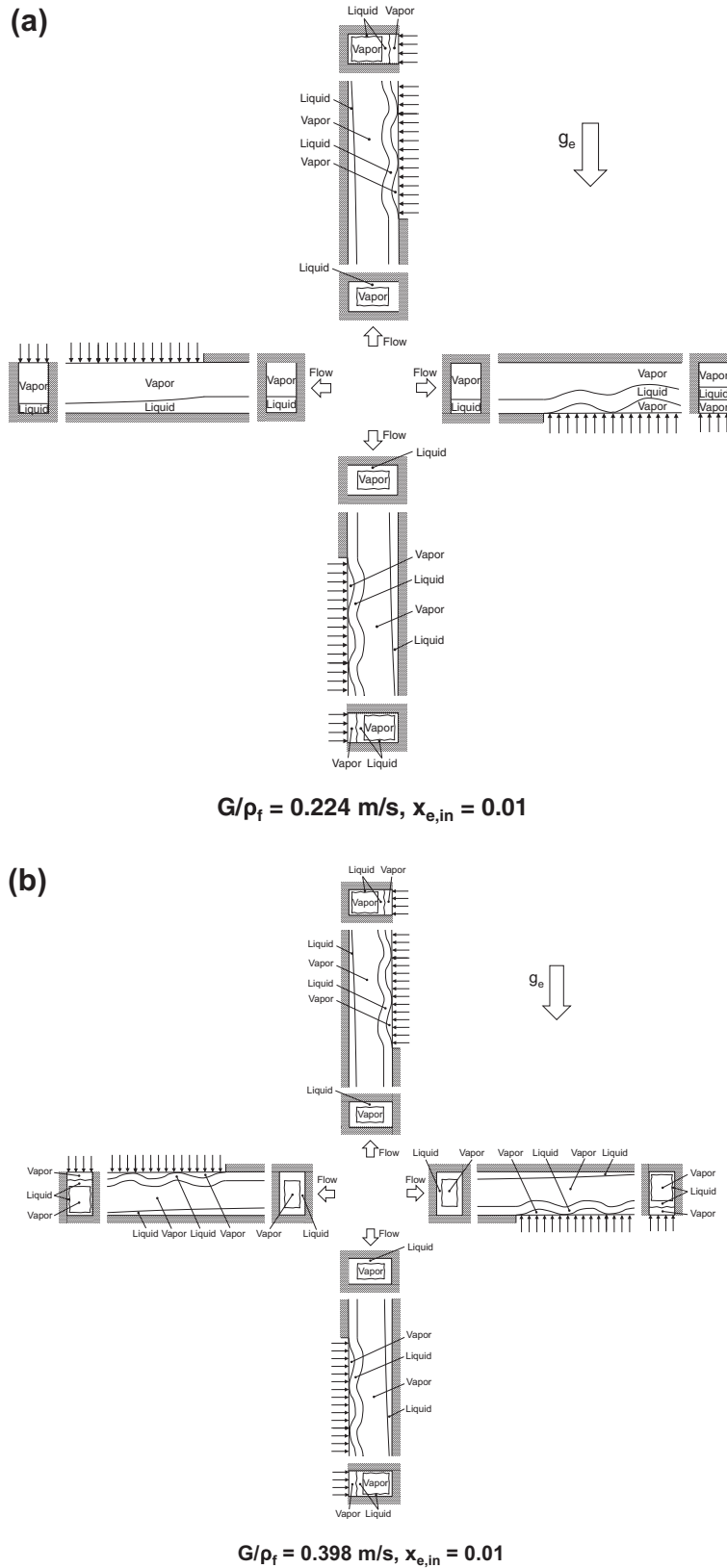**Fig. 5.** Schematic representation of interfacial behavior at CHF- for different flow orientations for (a) G/ρ_f = 0.224 m/s and $x_{e,in}$ = 0.01, and (b) G/ρ_f = 0.398 m/s and $x_{e,in}$ = 0.01.

mass velocity with G/ρ_f = 0.398 m/s and inlet quality of $x_{e,in}$ = 0.01. There appears to be appreciable diminution of the influence of buoyancy for all orientations. Here, interfacial behavior appears to be virtually identical for all orientations and similar to that for θ = 90° for the lower mass velocity in Fig. 4(a).

Figs. 5(a) and (b) show schematic diagrams representing interfacial behavior observed at CHF- for G/ρ_f = 0.224 and 0.398 m/s, respectively, at $x_{e,in}$ = 0.01. To simplify the schematic representations, only orientations corresponding to 90° orientation increments are shown. Cross-sectional depictions are provided for the

flow both upstream and downstream of the heated portion of the channel.

For G/ρ_f = 0.224 m/s, Fig. 5(a), and θ = 0°, the flow enters the channel stratified, with the vapor flowing above the liquid. At CHF-, intense vapor effusion at the heated wall begins to separate the liquid layer, ultimately causing unsteady rise in the wall temperature. At θ = 90°, the flow enters the channel with a thin liquid layer sheathing all four walls of the channel, surrounding a central vapor core. At CHF-, vapor effusion along the heated wall begins to separate the wall layer adjacent to the heated wall. Notice that, unlike the flow at θ = 0°, a thin liquid film continues to sheath the three insulated walls of the channel even at CHF-. At θ = 180°, the flow enters the channel stratified but unlike θ = 0°, the vapor is now adjacent to the heated wall. The heated wall receives minor cooling from remnants of liquid that are broken off the liquid layer and able to reach the top heated wall, but CHF is fairly small because of the limited access of liquid to the heated wall. For θ = 270°, the flow enters the channel separated, with a wall liquid layer surrounding a central vapor core. At CHF-, the momentum of vapor perpendicular to the heated wall causes separation of the liquid layer adjacent to the heated wall. Overall, the interfacial behavior at θ = 270° appears similar to that at θ = 90°, however, as will be discussed later, these orientations produce different CHF values because of the liquid shear and drag forces exerted in the same direction as buoyancy at θ = 90° but opposite to buoyancy at θ = 270°.

Fig. 5(b) shows schematics for CHF- at G/ρ_f = 0.398 m/s and $x_{e,in}$ = 0.01. Notice here that the interfacial behavior is similar for all orientations and reminiscent of that observed at θ = 90° for G/ρ_f = 0.224 m/s. This points to the effectiveness of high flow velocities at overcoming the influence of orientation. The similarity in interfacial behavior for different orientations at G/ρ_f = 0.398 m/s is indicative of (a) similarity in CHF mechanism and (b) diminution of the influence of orientation, but does not necessarily translate to equal CHF values for this mass velocity. This important issue of CHF magnitude will be discussed later.

As will be discussed later, the inlet region plays a crucial role in CHF development. Fig. 6 depicts video images of the inlet region for different orientations at $x_{e,in}$ = 0.01 and zero wall heat flux, 50% CHF and 95% CHF for G/ρ_f = 0.224 and 0.398 m/s. For the upward facing heated wall orientations, θ = 315, 0, and 45°, and zero heat flux, a vapor layer is shown residing above a liquid layer due to buoyancy. At 50% CHF, bubbles are shown nucleating and coalescing together within the liquid layer adjacent to the heated wall. Buoyancy appears to drive the coalescent bubbles to the liquid–vapor interface, where they are released into the vapor layer above. For the same orientations, there are visible differences between interfacial conditions at G/ρ_f = 0.224 m/s versus 0.398 m/s. The higher shear
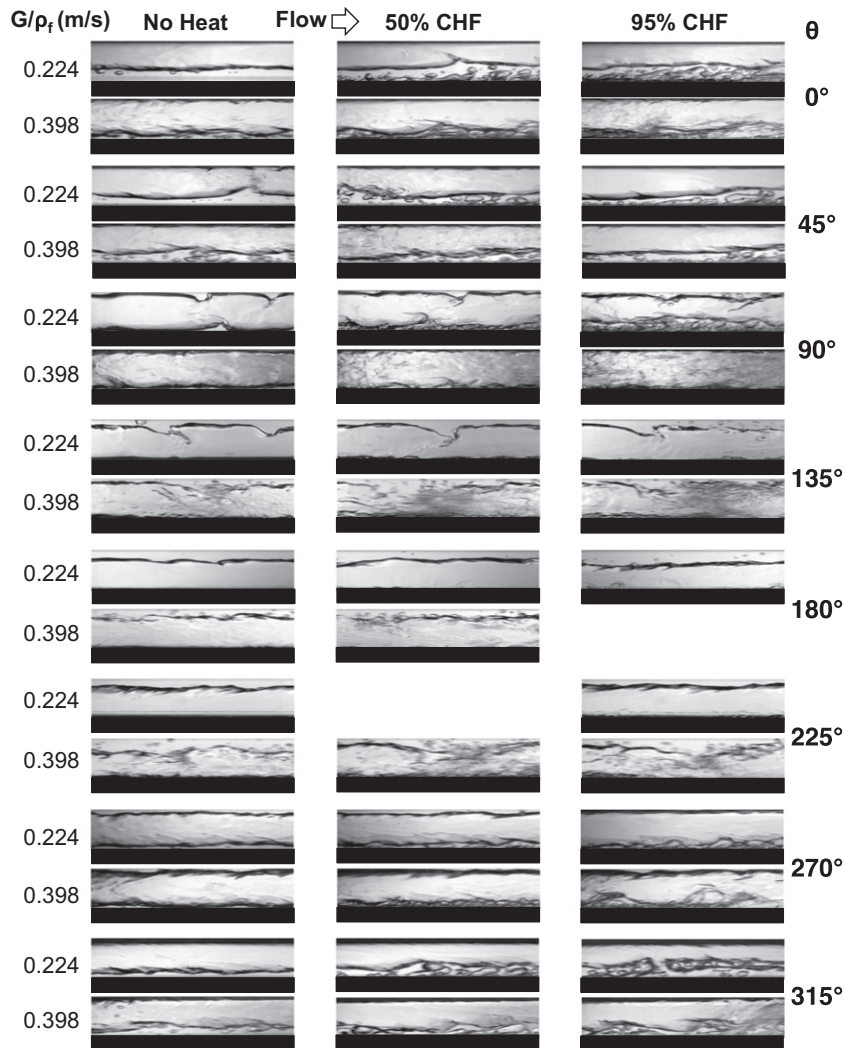

Fig. 6. Video images of flow boiling in inlet region for different orientations at $x_{e,in}$ = 0.01 and zero wall heat flux, 50% CHF and 95% CHF at G/ρ_f = 0.224 and 0.398 m/s. Missing images correspond to conditions for which video images are not available. The heated wall is indicated by a rectangular black strip.

stresses associated with the higher velocity appear to thin the heated wall liquid layer and cause axial stretching of the coalescent vapor layers. This behavior is indication of the aforementioned diminution of the influences of buoyancy and orientation in general on interfacial behavior. At 95% CHF, there is a clear separation of the liquid layer from the heated wall and formation of a vapor layer between the liquid and the heated wall. For the vertical upflow orientation, $\theta = 90°$, zero heating results in a flow pattern consisting of a liquid layer sheathing both the heated wall and opposite insulating wall, surrounding a central vapor core, with the interface of the liquid layer marred by roll waves, especially for $G/\rho_f = 0.224$ m/s. At 50% CHF, bubbles are shown forming in the liquid layer adjacent to the heated wall, coalescing together, and bursting into the vapor core. For the downward heated wall orientations, $\theta = 135°$, $180°$, and $225°$, with zero heat flux, a vapor layer is shown stratified by buoyancy against the heated wall above a liquid layer, with the interface in between marred by roll waves. Despite this stratification, remnants of liquid deposited from the wavy interface onto the heated wall appear to form thin patches of liquid along the heated wall. At 50% CHF, bubbles form along the heated wall within the liquid patches, which appear to serve as the sole, albeit weak source for wall cooling. At 95% CHF, there is appreciable loss of liquid at the heated wall because of the loss of liquid patches by evaporation. As discussed later, these orientations are associated with unusually low CHF values, especially for $G/\rho_f = 0.224$ m/s. For the vertical downflow orientation, $\theta = 270°$, the flow appears to resemble that for vertical upflow, $\theta = 90°$. However, given that the direction of buoyancy is opposite to that of liquid shear and drag forces for $\theta = 270°$, CHF values for $\theta = 270°$ are smaller than for $\theta = 90°$ as will be discussed next.

4. CHF results

Fig. 7(a) shows a polar plot of CHF data measured at all orientations for velocities ranging from $G/\rho_f = 0.126$ to 1.130 m/s and an inlet quality of $x_{e,in} = 0.01$. Notice how the influence of orientation is very pronounced for the two lowest velocities of $G/\rho_f = 0.126$ and

0.224 m/s, especially at $\theta = 225°$, where CHF values are vanishingly small. The middle velocity of $G/\rho_f = 0.398$ m/s marks the onset of diminution of orientation effects. The influence of orientation decreases further for the two higher velocities of $G/\rho_f = 0.712$ and 1.130 m/s, despite a persistent residual influence, with orientations involving a combination of upflow and/or upward-facing heated wall ($\theta = 0°$, $45°$ and $90°$) producing higher CHF than downflow and/or downward-facing heated wall ($\theta = 180°$, $225°$ and $270°$).

Fig. 7(b) shows a polar plot of CHF data for velocities ranging from $G/\rho_f = 0.126$ to 0.712 m/s at a much greater inlet quality of $x_{e,in} = 0.19$. Like Fig. 7(a), the influence of orientation for the lowest velocity of $G/\rho_f = 0.126$ m/s is very pronounced, yielding a vanishingly small CHF value for $\theta = 225°$. But unlike Fig. 7(a), the effect of orientation is noticeably weakened for $G/\rho_f = 0.224$ m/s at $x_{e,in} = 0.19$ compared to $x_{e,in} = 0.01$. The influence of orientation decreases further for the two higher velocities of $G/\rho_f = 0.398$ and 0.712, despite the afore-mentioned residual influence of orientation. Comparing Figs. 7(a) and (b) shows that, for equal G/ρ_f, increasing inlet quality reduces the sensitivity of CHF to orientation, which can be explained by the higher velocities of individual layers of the flow at higher $x_{e,in}$ greatly increasing the magnitude of shear and drag forces compared to buoyancy.

5. CHF prediction method

5.1. Determination of liquid and vapor layer velocities and thicknesses

As discussed earlier, CHF occurrence is a strong function of the relative magnitude of forces influencing the motion of individual liquid and vapor layers both along the channel and perpendicular to the heated wall. Determining the magnitude of these forces requires the determination of velocities and thicknesses of the individual layers. In this study, these parameters are determined using the control volume method, which consists of applying mass, momentum and energy conservation laws to control volumes encompassing the liquid and vapor phases separately as well as the combined flow. The control volume method proved highly
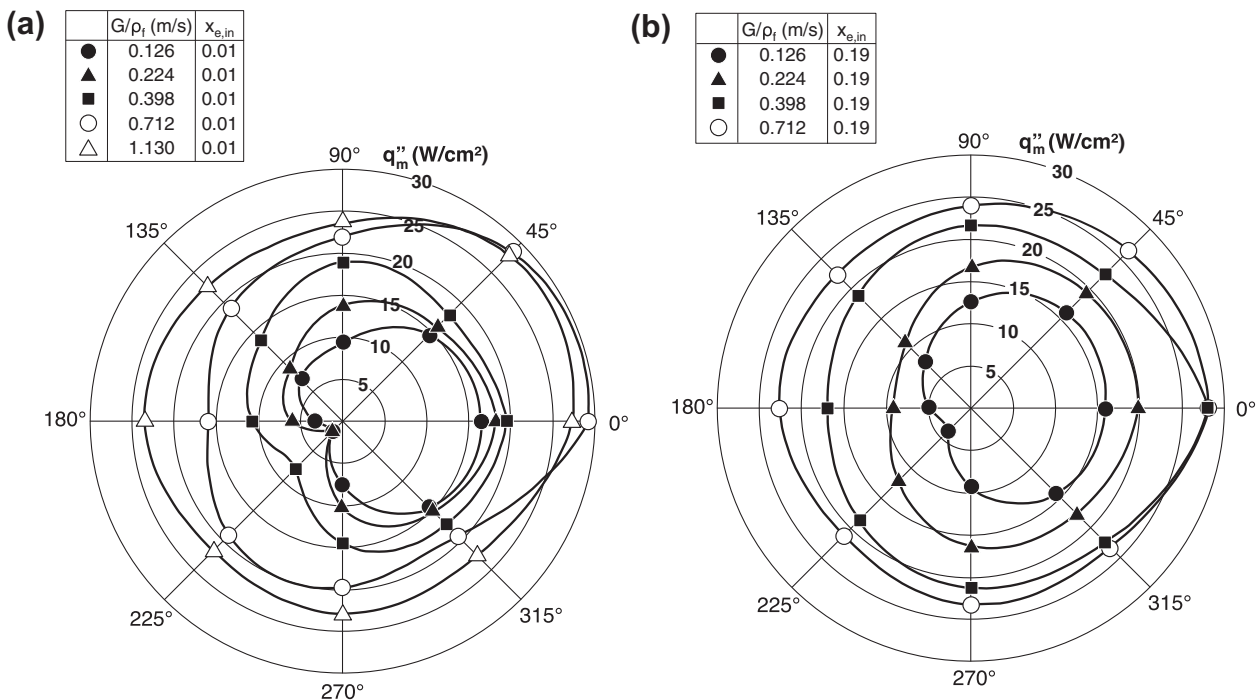

Fig. 7. Variation of CHF with orientation for different mass velocities at (a) $x_{e,in} = 0.01$ and (b) $x_{e,in} = 0.19$.

effective in predicting two-phase behavior for separated flows in several past studies [1,17,18,24,25,28–34].

The video images described earlier show different flow patterns prevailing at CHF- for different velocities, inlet qualities and orientations. Because of the long-term focus of this study of determining CHF for flow boiling in microgravity, as well as determining minimum flow conditions that would cause appreciable diminution of the influence of gravity, the present control volume analysis is based on the flow pattern depicted in Fig. 5(b), which is encountered at higher velocities irrespective of orientation.

The separated flow pattern observed at CHF- at relatively high velocities and depicted in Fig. 5(b) consists of a flow entering the channel with a liquid film sheathing all four channel walls surrounding a central vapor core. Along the heated wall, the liquid layer begins to separate from the wall as a vapor layer begins to form underneath. Fig. 8 shows a more detailed rendering of the same flow pattern, and identifies the individual layers of the separated flow along the heated wall: liquid layer 1 along the three adiabatic walls of the channel, central vapor layer 2, liquid layer 3 adjacent to, but separated from the heated wall, and vapor layer 4 at the heated wall beneath liquid layer 3. Unlike similar recent formulations by Kharangate et al. [29,30], the present separated flow model accounts for the varying influence of gravity for the different orientations.

The separated flow model is applied first to the adiabatic region upstream of the heated wall, and afterwards to the heated portion of the channel. For the adiabatic region, momentum conservation for the vapor and liquid portions of the channel yields

$$G^2 \frac{d}{dz}\left[\frac{x_{e,in}^2}{\rho_g \alpha_{in}}\right] = -\alpha_{in}\frac{dp}{dz} \pm \frac{\tau_i P_i}{A} - \rho_g \alpha_{in} g_e \sin\theta \quad (2)$$

and

$$G^2 \frac{d}{dz}\left[\frac{(1-x_{e,in})^2}{\rho_f(1-\alpha_{in})}\right] = -(1-\alpha_{in})\frac{dp}{dz} - \frac{\tau_{w,f}P_{w,f}}{A} \pm \frac{\tau_i P_i}{A} - \rho_f(1-\alpha_{in})g_e \sin\theta, \quad (3)$$

respectively, where $x_{e,in}$ is the inlet quality obtained from Eq. (1), α_{in} the inlet void fraction, $\tau_{w,f}$ the wall shear stress for the liquid layer, τ_i the interfacial shear stress, $P_{w,f}$ the channel perimeter, and P_i are the perimeter of liquid-vapor interface. The ± sign of the interfacial shear terms allows for any variations in the direction of the shear stress, depending on local velocity differences between the two layers.

Neglecting any property variations, mass and energy conservation result in $x_e = x_{e,in}$ for the adiabatic region. Eqs. (2) and (3) are solved simultaneously using an iterative procedure to determine a_{in}. Equations for the wall and interfacial shear stresses are similar to those utilized in the analysis of the heated section, which are discussed below. These stresses are functions of flow velocities, which are themselves functions of the void fraction.

Using Fig. 8 as a guide, the inlet mass flow fraction of liquid layer 1 along the insulated walls can be expressed in terms of the channel dimensions as

$$x_{f1,in} = \frac{W + 2H}{2W + 2H}(1 - x_{e,in}). \quad (4)$$

Similarly, the inlet mass flow fraction of liquid layer 3 can be expressed as

$$x_{f3,in} = \frac{W}{2W + 2H}(1 - x_{e,in}). \quad (5)$$

Because of the prevailing saturated conditions, heat transfer between the vapor core and the liquid layers is assumed negligible,
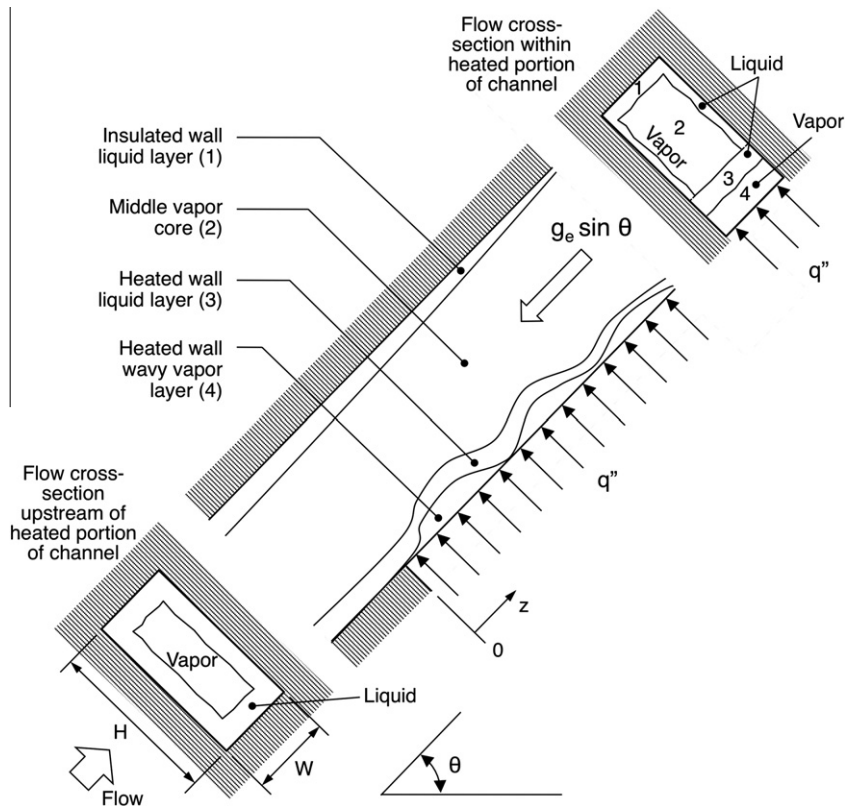

Fig. 8. Schematic of different separated layers at CHF- for high mass velocities.

which implies the flow quality of the vapor core is conserved ($x_2 = x_{e,in}$).

Similar relations are derived for the inlet area fraction of the liquid layer along the adiabatic walls (layer 1) and adjacent to heated wall (layer 3), respectively,

$$\varepsilon_{f1,in} = \frac{W + 2H}{2W + 2H}(1 - \alpha_{in}), \tag{6}$$

and

$$\varepsilon_{f3,in} = \frac{W}{2W + 2H}(1 - \alpha_{in}). \tag{7}$$

Applying conservation of mass for the entire heated section results in $d\dot{m}/dz = 0$, which implies both $\dot{m}$ and G are constant. Because of the prevailing saturated conditions, the temperature gradients between the four fluid layers are neglected. This implies the mass flow rates of the insulated wall liquid layer ($x_{f1} \dot{m}$) and central vapor core ($x_2 \dot{m}$) are both constant, which also implies that both x_{f1} and x_2 are constant. The growth of the vapor layer (4) in contact with the heated wall is the result of evaporation of the heated wall liquid layer (3), which implies $x_{f3} = x_{f3,in} - x_4$. Mass conservation yields the following relation for liquid evaporation rate along the interface between layers 3 and 4.

$$\dot{m}'_{fg} = GA\frac{dx_4}{dz}. \tag{8}$$

The next step in the implementation of the model is to apply momentum conservation to the insulated wall liquid layer (1), central vapor layer (2), heated wall liquid layer (3), and heated wall vapor layer (4), which yields, respectively,

$$G^2\frac{d}{dz}\left[\frac{x_{f1}^2}{\rho_f \varepsilon_{f1}}\right] = -\varepsilon_{f1}\frac{dp}{dz} - \frac{\tau_{w,f1}P_{w,f1}}{A} \pm \frac{\tau_{i12}P_{i12}}{A} \mp \frac{\tau_{i13}P_{i13}}{A}$$
$$- \rho_f \varepsilon_{f1}g_e \sin\theta, \tag{9}$$

$$G^2\frac{d}{dz}\left[\frac{x_2^2}{\rho_g \alpha_2}\right] = -\alpha_2\frac{dp}{dz} \mp \frac{\tau_{i12}p_{i12}}{A} \pm \frac{\tau_{i23}p_{i23}}{A} - \rho_g \alpha_2 g_e \sin\theta, \tag{10}$$

$$G^2\frac{d}{dz}\left[\frac{x_{f3}^2}{\rho_f(1 - \varepsilon_{f1} - \alpha_2 - \alpha_4)}\right] + \dot{m}'_{fg}u_{34}$$
$$= -(1 - \varepsilon_{f1} - \alpha_2 - \alpha_4)\frac{dp}{dz} - \frac{\tau_{w,f3}P_{w,f3}}{A} \pm \frac{\tau_{i13}P_{i13}}{A} \mp \frac{\tau_{i23}P_{i23}}{A}$$
$$\pm \frac{\tau_{i34}P_{i34}}{A} - \rho_f(1 - \varepsilon_{f1} - \alpha_2 - \alpha_4)g_e \sin\theta, \tag{11}$$

and

$$G^2\frac{d}{dz}\left[\frac{x_4^2}{\rho_g \alpha_4}\right] - \dot{m}'_{fg}u_{34} = -\alpha_4\frac{dp}{dz} - \frac{\tau_{w,g4}P_{w,g4}}{A} \mp \frac{\tau_{i34}P_{i34}}{A}$$
$$- \rho_g \alpha_4 g_e \sin\theta. \tag{12}$$

Table 1 provides relations for x_{f1}, x_2, x_{f3} and x_4 that are used in the above equations. In Eqs. (9)–(12), $\tau_{w,f1}$, $\tau_{w,f3}$, $\tau_{w,g4}$ are, respectively, the wall shear stresses for the insulated wall liquid layer, heated wall liquid layer, and heated wall vapor layer, and τ_{i12}, τ_{i13}, τ_{i23}, and τ_{i34} are the interfacial shear stresses between the insulated wall liquid layer and vapor core, insulated wall liquid layer and heated wall liquid layer, vapor core and heated wall liquid layer, and heated wall liquid layer and heated wall vapor layer, respectively, $P_{w,f1}$, $P_{w,g2}$, $P_{w,f3}$, and $P_{w,g4}$ are the wall perimeters of the insulated wall liquid layer, vapor core, heated wall liquid layer, and heated wall vapor layer, respectively, P_{i12}, P_{i13}, P_{i23}, and P_{i34} are the interfacial perimeters between the insulated wall liquid layer and vapor core, insulated wall liquid layer and heated wall liquid layer, vapor core and heated wall liquid layer, and heated wall liquid layer and heated wall vapor layer, respectively.

The vapor generated at the heated wall is assumed to have no initial stream-wise velocity [29], therefore contributing no stream-wise momentum to the adjacent heated liquid layer. Relations for the wall shear stress for each phase are provided in Table 1. Also included in Table 1 are relations for all the interfacial shear stresses.

Applying energy conservation to a control volume encompassing the entire cross-sectional area of the channel yields

$$\frac{dx}{dz} = \frac{dx_4}{dz} = \frac{q''W}{\dot{m}h_{fg}}. \tag{13}$$

5.2. Hydrodynamic instability of liquid–vapor interface along the heated wall

As depicted in Fig. 5(b), CHF for high velocities is preceded by the formation of a wavy vapor layer beneath the heated wall liquid layer. Velocity differences between the two layers result in instability of the interface in-between. Therefore conditions at CHF-can be described by classical instability theory [15,36,37]. As shown in Fig. 9(a), deformation of the liquid-vapor interface is assumed to follow the sinusoidal wave form

$$\eta(z, t) = \eta_o e^{ik(z - ct)}. \tag{14}$$

Table 1
Summary of relations used in conjunction with the control volume model.

Quality relations for individual layers:

$$x_{f1} = \frac{\rho_f U_{f1} \varepsilon_{f1}}{G}, \quad x_2 = \frac{\rho_g U_{g2} \alpha_2}{G} = x_{e,in}, \quad x_{f3} = \frac{\rho_f U_{f3}(1 - \varepsilon_{f1} - \alpha_2 - \alpha_4)}{G}, \quad x_4 = \frac{\rho_g U_{g4} \alpha_4}{G}$$

Wall shear stress relations:

$$\tau_{w,kj} = \frac{1}{2}\rho_k U_{k,j}^2 f_{k,j}$$

$$f_{k,j} = C_1 + \frac{C_2}{\mathrm{Re}_{D,k,j}^{1/C_3}} = C_1 + \frac{C_2}{\left(\frac{\rho_k U_{k,j} D_{k,j}}{\mu_k}\right)^{1/C_3}}$$

where $k = f$ or g, and $j = 1$–4. $C_1 = 0$, $C_2 = 16$ and $C_3 = 1$ for laminar flow ($\mathrm{Re}_{D,k,j} \leqslant 2100$), $C_1 = 0.0054$, $C_2 = 2.3 \times 10^{-8}$ and $C_3 = -2/3$ for transitional flow ($2100 < \mathrm{Re}_{D,k,j} \leqslant 4000$), and $C_1 = 0.00128$, $C_2 = 0.1143$ and $C_3 = 3.2154$ for turbulent flow ($\mathrm{Re}_{D,k,j} > 4000$) [35], where $D_{k,j} = 4A_{k,j}/P_{k,j}$

Interfacial shear stress relations:

$$\tau_{i12} = \frac{C_{f,i}}{2}\rho_g(U_{f1} - U_{g2})^2, \quad \tau_{i23} = \frac{C_{f,i}}{2}\rho_g(U_{g2} - U_{f3})^2, \quad \tau_{i34} = \frac{C_{f,i}}{2}\rho_g(U_{f3} - U_{g4})^2, \tau_{i13} = \frac{C_{f,i}}{2}\rho_g(U_{f1} - U_{f3})^2$$

where $C_{f,i} = 0.5$ [25]
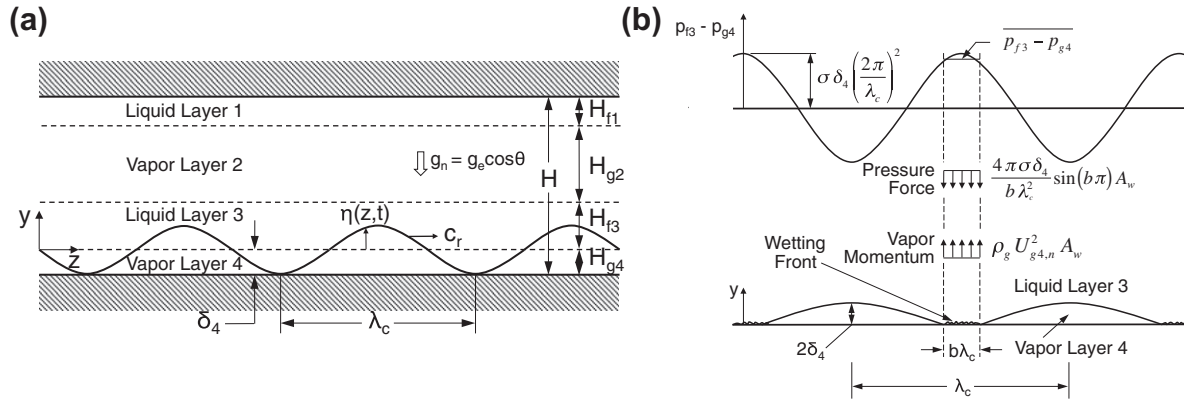
(a)

(b)

Fig. 9. Schematics of interfacial lift-off model: (a) wavy vapor layer formation along heated wall at CHF-, and (b) interfacial lift-off of wetting front at CHF.

where η_o represents the wave amplitude ($\eta_o = \delta$), k the wave number ($k = 2\pi/\lambda$), and c the wave speed. The real part of Eq. (14) represents the actual liquid–vapor interface while the imaginary part is used to establish a criterion for interfacial instability. Any perturbation normal to the interface produces a pressure difference across the interface that can be expressed as

$$p_{f3} - p_{g4} = -\left[\rho_{f3}''(c - U_{f3})^2 + \rho_{g4}''(c - U_{g4})^2 + (\rho_f - \rho_g)\frac{g_n}{k}\right]k\eta_o e^{ik(z-ct)},$$
(15)

where $\rho_{f3}'' = \rho_f \coth(kH_{f3})$ and $\rho_{g4}'' = \rho_g \coth(kH_{g4})$, which are 'modified density' terms, and g_n is the component of gravity acting normal to the heated wall. The mean liquid and vapor thicknesses, H_{f3} and H_{g4}, found in the modified density terms are obtained from the control volume model and are given, respectively, by

$$H_{f3} = (1 - \varepsilon_{f1} - \alpha_2 - \alpha_4)H$$
(16)

and

$$H_{g4} = \alpha_4 H.$$
(17)

The pressure difference across the interface is balanced by the surface tension force,

$$p_f - p_g \approx \sigma \frac{\partial^2 \eta}{\partial z^2} = -\sigma \eta_o k^2 e^{ik(z-ct)}.$$
(18)

Combining Eqs. (15) and (18) yields the following expression for the wave speed,

$$c = \frac{\rho_{f3}'' U_{f3} + \rho_{g4}'' U_{g4}}{\rho_{f3}'' + \rho_{g4}''}$$
$$\pm \sqrt{\frac{\sigma k}{\rho_{f3}'' + \rho_{g4}''} - \frac{\rho_{f3}'' \rho_{g4}''(U_{g4} - U_{f3})^2}{(\rho_{f3}'' + \rho_{g4}'')^2} - \frac{(\rho_f - \rho_g)}{(\rho_{f3}'' + \rho_{g4}'')}\frac{g_e \cos\theta}{k}},$$
(19)

where the terms under the radical represent the effects of different momentum or force terms. The first term accounts for the surface tension force, and this effect is always stabilizing to the interface. The second term accounts for velocity difference between the heated vapor and liquid layers, which is destabilizing. The third term accounts for the effect of the component of gravity perpendicular to the heated wall, and this effect is stabilizing when the flow orientation places the vapor above the liquid, and destabilizing otherwise.

Should the destabilizing effects in Eq. (19) become dominant, the expression under the radical become negative, and the wave speed acquires both real and imaginary components, $c = c_r + i\, c_i$, where the imaginary component is given by

$$c_i = \sqrt{\frac{\rho_{f3}'' \rho_{g4}''(U_{g4} - U_{f3})^2}{(\rho_{f3}'' + \rho_{g4}'')^2} + \frac{(\rho_f - \rho_g)}{(\rho_{f3}'' + \rho_{g4}'')}\frac{g_e \cos\theta}{k} - \frac{\sigma k}{\rho_{f3}'' + \rho_{g4}''}},$$
(20)

The critical wavelength, λ_c, defined as the wavelength of a neutrally stable wave ($c_i = 0$), can be determined by setting the radical in Eq. (20) equal to zero.

$$k_c = \frac{2\pi}{\lambda_c} = \frac{\rho_{f3}'', \rho_{g4}''(U_{g4} - U_{f3})^2}{2\sigma(\rho_{f3}'' + \rho_{g4}'')}$$
$$+ \sqrt{\left[\frac{\rho_{f3}'' \rho_{g4}''(U_{g4} - U_{f3})^2}{2\sigma(\rho_{f3}'' + \rho_{g4}'')}\right]^2 + \frac{(\rho_f - \rho_g)g_e \cos\theta}{\sigma}}.$$
(21)

One important practical implication of Eq. (21) is that for very high velocity conditions, λ_c will approach the limit

$$\lambda_c = \frac{2\pi\sigma(\rho_{f3}'' + \rho_{g4}'')}{\rho_{f3}'' \rho_{g4}''(U_{g4} - U_{f3})^2}.$$
(22)

irrespective of body force, which is consistent with the trend of CHF versus orientation for high velocities depicted in Figs. 7(a) and (b).

5.3. Modified interfacial lift-off criterion

The interfacial lift-off model recently presented by Kharangate [29] is modified to account for the effects of body force. CHF is postulated to occur when the momentum of vapor emanating from wetting fronts on the heated wall overcomes the pressure force caused by the interfacial curvature. This results in the interface in the wetting front detaching from the heated wall, which precludes any further liquid access within the wetting front. The heat flux in the surrounding wetting fronts increases to compensate for the reduced liquid access. The surrounding wetting fronts now become more prone to lift-off because of the increased normal vapor momentum. Eventually more wetting fronts are lifted, preventing any appreciable liquid access to the heated wall, and CHF ensues.

Illustrated in Fig. 9(b), the lift-off flux is determined by equating the pressure force pushing the interface towards the heated wall to the vapor momentum pushing the interface away from the heated wall. The vapor momentum $\rho_g U_{g4,n}^2$ emanating from a wetting front of length $b\lambda_c$ is opposed by the pressure difference

$$\overline{p_{f3} - p_{g4}} = \frac{4\pi\sigma\delta_4}{b\lambda^2}\sin(b\pi).$$
(23)

Previous studies [38] have shown that the ratio of wetting front length to critical wavelength is given by $b = 0.2$. The velocity of vapor in the wetting front normal to the heated wall can be determined by equating the heat input from the wall through the wetting front to the latent heat of the normal vapor flow.

$$q''_w A_w = \rho_g U_{g4,n} A_w h_{fg}, \tag{24}$$

where A_w is the area of the wetting front. Equating the vapor momentum, $\rho_g U_{g4,n}^2$, to the pressure difference given by Eq. (23), and introducing Eq. (24), yield the following expression for the lift-off heat flux in the wetting front,

$$q''_w = \rho_g h_{fg} \sqrt{\frac{p_{f3} - p_{g4}}{\rho_g}} = \rho_g h_{fg} \left[\frac{4\pi\sigma}{\rho_g} \frac{\sin(b\pi)}{b} \right]^{1/2} \frac{\delta^{1/2}}{\lambda_c}. \tag{25}$$

The critical heat flux, q''_m, is based on the entire heated area. Because the heat flux, q''_w, in Eq. (25) is based on wetting front area, CHF can be determined from the relation

$$q''_m = b q''_w. \tag{26}$$

Previous studies [38] proved the existence of a continuous upstream wetting region, z^*, defined as $z^* = z_o + \lambda_c(z^*)$, where z_o is the distance from the leading edge of the heated wall to the location where the vapor velocity just overcomes the liquid velocity. Hydrodynamic instability generates the wavy interface at z^*, downstream from which the wavy vapor layer begins to propagate along the heated wall.

Combining Eqs. (25) and (26) gives the following relation for CHF,

$$q''_m = \rho_g h_{fg} \left[\frac{4\pi\sigma b \sin(b\pi)}{\rho_g} \right]^{1/2} \frac{\delta_4^{1/2}}{\lambda_c} \Bigg|_{z^*}. \tag{27}$$

where, as discussed earlier, $b = 0.2$, and δ_4 is the thickness of vapor layer 4; both δ_4 and λ_c are calculated at z^*.
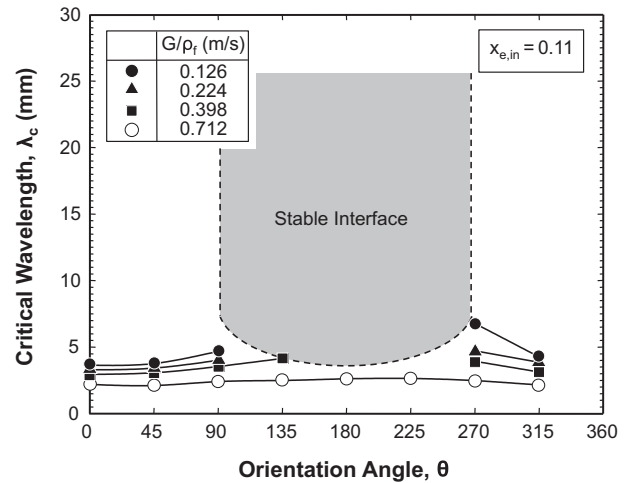

Fig. 11. Variation of predicted critical wavelength at z^*, calculated using measured CHF, for $x_{e,in} = 0.11$.

Calculation of CHF using a combination of the control volume model and the interfacial lift-off model requires an iterative numerical scheme. Key inputs for the control volume model are mass velocity, G, pressure at the inlet to the heated wall, p_{in}, inlet quality, $x_{e,in}$, and inlet void fraction α_{in}. This scheme is initiated with a guessed value for CHF, which is used in the control volume model to predict the velocities and area fractions for all four layers of the flow for every Δz axial increment from the upstream edge of
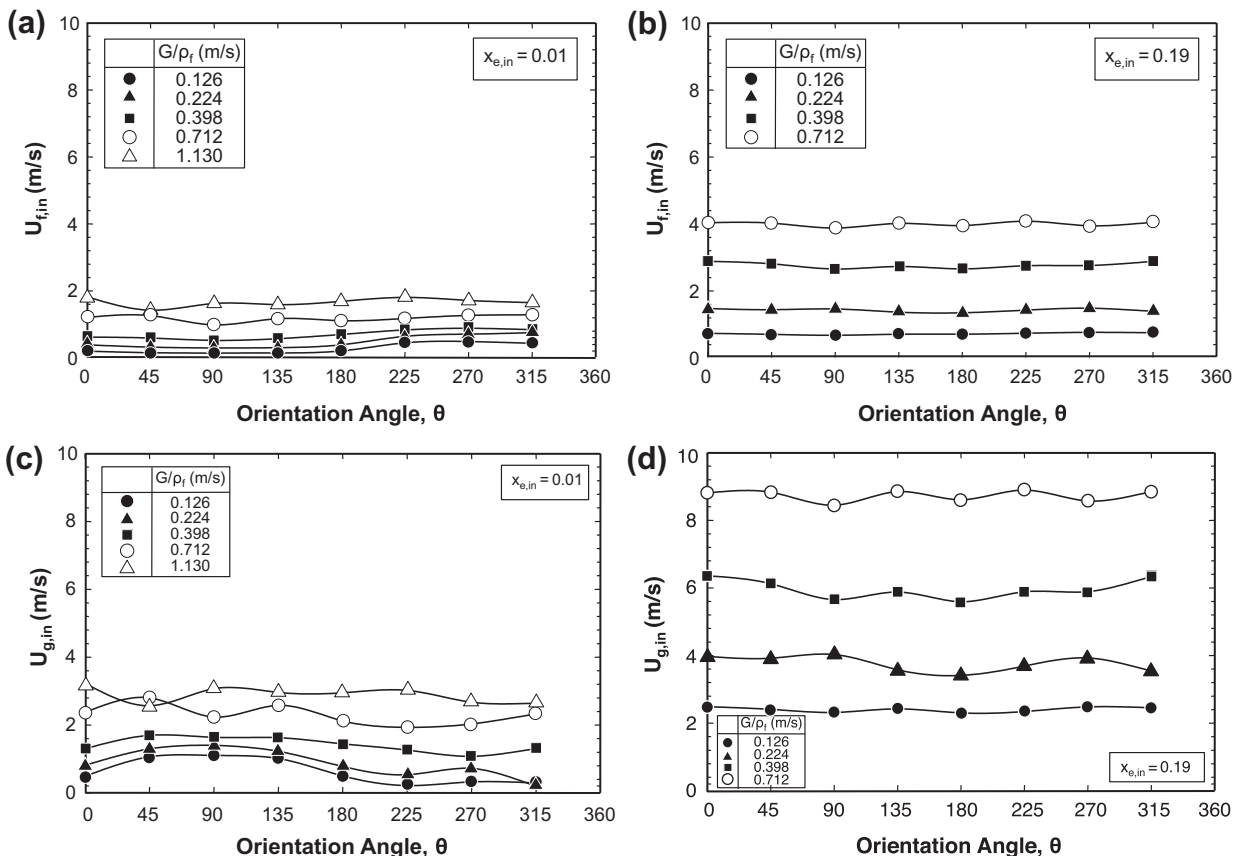

Fig. 10. Variation of predicted mean liquid velocity at inlet to heated wall for (a) $x_{e,in} = 0.01$ and (b) $x_{e,in} = 0.19$, and predicted mean vapor velocity for (c) $x_{e,in} = 0.01$ and (d) $x_{e,in} = 0.19$.
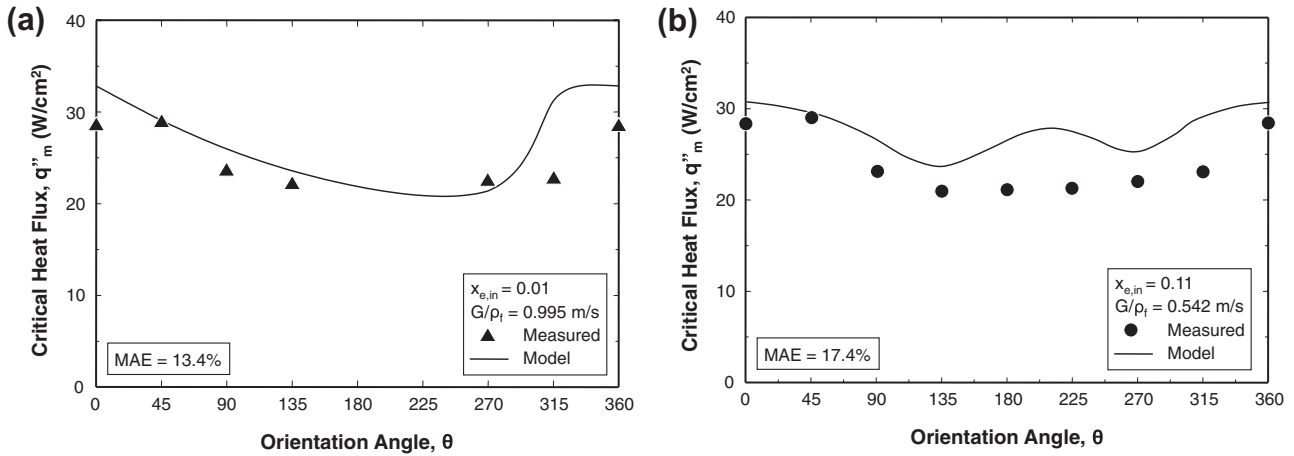
Fig. 12. Comparison of measured and predicted CHF for: (a) $x_{e,in} = 0.01$ and $G/\rho_f = 0.995$ m/s, and (b) $x_{e,in} = 0.11$ and $G/\rho_f = 0.542$ m/s.

the heated wall. The control volume model relations are solved simultaneously along the heated wall with the aid of a 4-th order Runge–Kutta numerical scheme using saturated fluid properties that are updated for each Δz increment based on local pressure. The outputs of the control volume model are then used in the instability analysis to determine the critical wavelength, λ_c, and z^*, which requires another series of iterations. Finally, the calculated parameters are used in Eq. (27) to calculate a new CHF value. The entire calculation scheme is now repeated using the newly calculated CHF value. Further iteration is attempted until the CHF value used in the control volume model and predicted CHF value converge.

6. Model predictions

Figs. 10(a) and (b) show predictions of the liquid layer velocity at the inlet to the heated portion of the channel, $U_{f,in}$, for $x_{e,in} = 0.01$ and $x_{e,in} = 0.19$, respectively. Because the flow enters the channel as a two-phase mixture, the mixture density is significantly smaller than the liquid density. This yields a liquid velocity significantly greater than G/ρ_f, which is the mean velocity for pure liquid at the inlet. Comparing Figs. 10(a) and (b) shows the liquid velocity increases with increasing $x_{e,in}$ because of the significantly lower mixture density at higher $x_{e,in}$. Notice that there is appreciable influence of flow orientation on $U_{f,in}$ for $x_{e,in} = 0.01$ and $G/\rho_f = 0.126$ and 0.224 m/s, but this influence is much weaker for $x_{e,in} = 0.01$ and $G/\rho_f = 0.712$ and 1.130 m/s. For $x_{e,in} = 0.19$, the influence of orientation is fairly weak for the entire range of G/ρ_f. These trends can be explained by the dominance of fluid inertia compared to buoyancy as $x_{e,in}$ and G/ρ_f are increased.

Figs. 10(c) and (d) show predictions of the vapor core velocity at the inlet to the heated portion of the channel, $U_{g,in}$, for $x_{e,in} = 0.01$ and $x_{e,in} = 0.19$, respectively. Here too, the vapor velocity is significantly greater than G/ρ_f, especially for $x_{e,in} = 0.19$, and the influence of flow orientation is fairly weak for $G/\rho_f = 0.712$ and 1.130 m/s at $x_{e,in} = 0.01$, and for the entire range of G/ρ_f at $x_{e,in} = 0.19$.

Fig. 11 shows the variation of critical wavelength, λ_c, with flow orientation for an intermediate inlet quality value of $x_{e,in} = 0.11$. The critical wavelength is determined using Eq. (21) with the liquid and vapor velocities and different layer thicknesses predicted by the separated flow model at z^* using measured CHF values. It is important to note that hydrodynamic instability of the liquid-vapor interface adjacent to the heated wall is crucial to maintaining the wetting fronts that provide liquid access to the wall. Notice in Fig. 11 the existence of a broad region of flow orientations be-

tween $\theta = 90°$ and $270°$ and low values of G/ρ_f, where the interface is stable. This region encompasses downward-facing heated wall orientations, where buoyancy causes stratification of vapor towards the heated wall, and CHF values are comparatively small. The interfacial lift-off model is valid for velocities and orientations where the interface is unstable. For the unstable region, the wavelength increases with decreasing G/ρ_f, meaning wetting fronts are remote from one another for low velocities. Notice how the highest velocity of $G/\rho_f = 0.712$ m/s produces two important effects: (a) an unstable interface for all flow orientations, and (b) greatly reduced sensitivity of the critical wavelength to flow orientation. This demonstrates the importance of inertia at overcoming buoyancy effects and helping produce CHF values that are insensitive to flow orientation.

As indicated earlier, the interfacial lift-off model is valid for flow conditions and orientations that produce an unstable interface and the separated four-layer flow pattern depicted in Fig. 5(b). This excludes low velocities especially in combination with orientations associated with downflow and downward-facing heated wall.

Figs. 12(a) and (b) compare the model predictions with experimental data for two operating conditions: $G/\rho_f = 0.995$ m/s and $x_{e,in} = 0.01$, and $G/\rho_f = 0.542$ and $x_{e,in} = 0.11$, respectively, and all orientations. These plots show good agreement in both trend and magnitude, evidenced by MAE values of 13.4% and 17.4%, respectively, where

$$MAE = \frac{1}{M} \sum \frac{|q''_{m,exp} - q''_{m,pred}|}{q''_{m,exp}} \times 100\%. \qquad (28)$$

Notice how CHF is highest for $\theta = 0° - 45°$ and $315° - 360°$, orientations that produce a buoyancy force that assists vapor removal and liquid replenishment at the heated wall. Conversely, CHF is lowest for $\theta = 135° - 225°$, where buoyancy promotes vapor blanketing of the heated wall and hinders the liquid replenishment.

In a previous study by Zhang et al. [17,18] involving flows with zero inlet quality, the interfacial lift-off mechanism was shown to be dominant for relatively higher velocities at all flow orientations. In a later study by Zhang et al. [1] involving flows with zero inlet quality in microgravity, the interfacial lift-off mechanism was proven dominant for both low and high velocities in the absence of a body force. The present study demonstrates the validity of the interfacial lift-off mechanism for different orientations at relatively high velocities at 1 g_e. Future work will involve testing of the flow boiling module in microgravity to determine if the same mechanism is valid for all velocities. A key objective of the microgravity experiments to determine the flow rate threshold above which

CHF values in microgravity are identical to those measured at 1 g_e. The importance of such assessment is that, by exceeding the threshold flow rate, any models or data developed from ground-based $1 - g_e$ studies can be employed with confidence for design of reduced gravity and microgravity thermal management systems.

7. Conclusions

This study explored flow boiling CHF for FC-72 in a rectangular channel fitted along one side with a heated wall. The flow was supplied as a two-phase mixture and the channel was tested at different orientations relative to Earth's gravity. High-speed video imaging was used to explore interfacial behavior at heat fluxes up to and including CHF to capture the CHF trigger mechanism for different orientations, mass velocities and inlet qualities. The CHF data were compared to predictions of the interfacial lift-off model. Key findings from the study are as follows.

(1) For low mass velocities ($G/\rho_f \leqslant 0.224$ m/s) and small inlet qualities, orientation has a significant influence on CHF. The orientations surrounding horizontal flow with upward-facing heated wall cause buoyancy to separate the flow with liquid flowing along the heated wall and the vapor flowing above. CHF for these orientations is triggered when intense vapor production separates the liquid layer from the heated wall. On the other hand, orientations surrounding horizontal flow with downward-facing heated wall cause stratification of the vapor towards the heated wall and yield very small CHF values.

(2) High mass velocities ($G/\rho_f \geqslant 0.398$ m/s) cause appreciable diminution in the influence of orientation on CHF, which is evidenced by similar flow separation patterns and CHF trigger mechanism regardless of orientation. This behavior can be explained by the higher mass velocities increasing the magnitude of shear and drag forces compared to buoyancy, especially for high inlet qualities.

(3) Excluding the combination of very low velocities and downward-facing heated wall orientations, the influence of orientation on CHF is predicted with good accuracy in both trend and magnitude by the interfacial lift-off model. The model points to the effectiveness of inertia at overcoming buoyancy effects and helping produce CHF values insensitive to orientation.

Acknowledgement

References

[1] H. Zhang, I. Mudawar, M.M. Hasan, Flow boiling CHF in microgravity, Int. J. Heat Mass Transfer 48 (2005) 3107–3118.

[2] F.P. Chiaramonte, J.A. Joshi, Workshop on critical issues in microgravity fluids, transport, and reaction processes in advanced human support technology – final report, NASA TM-2004-212940, 2004.

[3] The National Academies, Recapturing a Future for Space Exploration: Life and Physical Sciences Research for a New Era, National Academics Press, Washington, DC, 2011.

[4] I. Mudawar, Two-phase micro-channel heat sinks: theory, applications and limitations, ASME J. Electron. Packag. 133 (2011). 041002-2.

[5] I. Mudawar, K.A. Estes, Optimizing and predicting CHF in spray cooling of a square surface, ASME J. Heat Transfer 118 (1996) 672–680.

[6] L. Lin, R. Ponnappan, Heat transfer characteristics of spray cooling in a closed loop, Int. J. Heat Mass Transfer 46 (2003) 3737–3746.

[7] J.R. Rybicki, I. Mudawar, Single-phase and two-phase cooling characteristics of upward-facing and downward-facing sprays, Int. J. Heat Mass Transfer 49 (2006) 5–16.

[8] Y. Katto, M. Kunihiro, Study of the mechanism of burn-out in boiling system of high burn-out heat flux, Bull. JSME 16 (1973) 1357–1366.

[9] I. Mudawar, D.C. Wadsworth, Critical heat flux from a simulated electronic chip to a confined rectangular impinging jet of dielectric liquid, Int. J. Heat Mass Transfer 34 (1991) 1465–1480.

[10] D.C. Wadsworth, I. Mudawar, Enhancement of single-phase heat transfer and critical heat flux from an ultra-high-flux simulated microelectronic heat source to a rectangular impinging jet of dielectric liquid, ASME J. Heat Transfer 114 (1992) 764–768.

[11] M.E. Johns, I. Mudawar, An ultra-high power two-phase jet-impingement avionic clamshell module, ASME J. Electron. Packag. 118 (1996) 264–270.

[12] T.C. Willingham, I. Mudawar, Forced-convection boiling and critical heat flux from a linear array of discrete heat sources, Int. J. Heat Mass Transfer 35 (1992) 2879–2890.

[13] M.B. Bowers, I. Mudawar, High flux boiling in low flow rate, low pressure drop mini-channel and micro-channel heat sinks, Int. J. Heat Mass Transfer 37 (1994) 321–332.

[14] T.N. Tran, M.W. Wambsganss, D.M. France, Small circular- and rectangular-channel boiling with two refrigerants, Int. J. Multiphase Flow 22 (1996) 485–498.

[15] H.J. Lee, S.Y. Lee, Heat transfer correlation for boiling flows in small rectangular horizontal channels with low aspect ratios, Int. J. Multiphas Flow 27 (2001) 2043–2062.

[16] V. Khanikar, I. Mudawar, T. Fisher, Effects of carbon nanotube coating on flow boiling in a micro-channel, Int. J. Heat Mass Transfer 52 (2009) 3805–3817.

[17] H. Zhang, I. Mudawar, M.M. Hasan, Experimental assessment of the effects of body force, surface tension force, and inertia on flow boiling CHF, Int. J. Heat Mass Transfer 45 (2002) 4079–4095.

[18] H. Zhang, I. Mudawar, M.M. Hasan, A method for assessing the importance of body force on flow boiling CHF, ASME J. Heat Transfer 126 (2004) 161–168.

[19] S.S. Kutateladze, A.I. Leont'ev, Some applications of the asymptotic theory of the turbulent boundary layer, in: Proceedings 3rd International Heat Transfer Conference, Chicago, Illinois, vol. 3, 1966, p. 1–6.

[20] L.S. Tong, Boundary-layer analysis of the flow boiling crisis, Int. J. Heat Transfer 11 (1968) 1208–1211.

[21] W. Hebel, W. Detavernier, M. Decreton, A contribution to the hydrodynamics of boiling crisis in a forced flow of water, Nuclear Eng. Design 64 (1981) 443–445.

[22] J. Weisman, B.S. Pei, Prediction of critical heat flux in flow boiling at low qualities, Int. J. Heat Mass Transfer 26 (1983) 1463–1477.

[23] C.H. Lee, I. Mudawar, A mechanistic critical heat flux model for subcooled flow boiling based on local bulk flow conditions, Int. J. Multiphase Flow 14 (1988) 711–728.

[24] J.E. Galloway, I. Mudawar, CHF mechanism in flow boiling from a short heated wall – Part 1. Examination of near-wall conditions with the aid of photomicrography and high-speed video imaging, Int. J. Heat Mass Transfer 36 (1993) 2511–2526.

[25] J.E. Galloway, I. Mudawar, CHF mechanism in flow boiling from a short heated wall – Part 2. Theoretical CHF model, Int. J. Heat Mass Transfer 36 (1993) 2527–2540.

[26] R.J. Simoneau, F.F. Simon, A visual study of velocity and buoyancy effects on boiling Nitrogen, NASA Tech Note TN D-3354, 1966.

[27] K. Mishima, H. Nishihara, The effect of flow direction and magnitude on CHF for low pressure water in thin rectangular channels, Nuclear Eng. Design 86 (1985) 165–181.

[28] C.O. Gersey, I. Mudawar, Orientation effects on critical heat flux from discrete, in-line heat sources in a flow channel, ASME J. Heat Transfer 115 (1993) 973–985.

[29] C.R. Kharangate, I. Mudawar, M.H. Hasan, Experimental and theoretical study of critical heat flux in vertical upflow with inlet vapor void, Int. J. Heat Mass Transfer 55 (2012) 360–374.

[30] C.R. Kharangate, I. Mudawar, M.H. Hasan, Photographic study and modeling of critical heat flux in horizontal flow boiling with inlet vapor void, Int. J. Heat Mass Transfer 55 (2012) 4154–4168.

[31] I. Mudawar, A.H. Howard, C.O. Gersey, An analytical model for near-saturated pool boiling CHF on vertical surfaces, Int. J. Heat Mass Transfer 40 (1997) 2327–2339.

[32] A.H. Howard, I. Mudawar, Orientation effects on pool boiling CHF and modeling of CHF for near-vertical surfaces, Int. J. Heat Mass Transfer 42 (1999) 1665–1688.

[33] J.C. Sturgis, I. Mudawar, Critical heat flux in a long, rectangular channel subjected to onesided heating – I. Flow visualization, Int. J. Heat Mass Transfer 42 (1999) 1835–1847.

[34] J.C. Sturgis, I. Mudawar, Critical heat flux in a long, rectangular channel subjected to onesided heating – II. Analysis of critical heat flux data, Int. J. Heat Mass Transfer 42 (1999) 1849–1862.

[35] M.S. Bhatti, R.K. Shah, Turbulent and transitional convective heat transfer in ducts, in: S. Kakac, R.K. Shah, R.k., W. Aung (eds.), Handbook of Single-phase Convective Heat Transfer, John Wiley and Sons, NY, 1987.

[36] H. Lamb, Hydrodynamics, sixth ed., Dover Publications, NY, 1945.

[37] L.M. Milne-Thompson, Theoretical Hydrodynamics, fourth ed., Macmillan, NY, 1960.

[38] H. Zhang, I. Mudawar, M.M. Hasan, CHF model for subcooled flow boiling in Earth gravity and microgravity, Int. J. Heat Mass Transfer 50 (2007) 4039–4051.